Chapter 3

Cascaded Ultrafast Energy Redistribution of an Intramolecular HB

The ultrafast hydrogen bond dynamics has been extensively studied in the last two decades. Powerful IR lasers with a duration on a subpicosecond time scale facilitated investigation of vibrational motions and enabled to get an insight into the strength of intra and intermolecular couplings, which is the key to understanding the mechanisms of many processes occurring in nature. Experiments have proven that the hydrogen bond dynamics is a multi-dimensional process ([19],[86]-[88]), i.e., the hydrogen motion is coupled to the skeleton vibrations. Any theoretical modelling has to account for this fact. While slow processes such as proton tunnelling are reasonably described within the Born-Oppenheimer scheme using an adiabatic approximation to the multi-dimensional motion, ultrafast laser driven dynamics necessarily comes along with a complex behavior including nonadiabatic transitions and related ultrafast IVR, for instance.

Coherent vibrational motion of a hydrogen bonded system had been observed for the first time by Stenger et al. [19]: One - color pump - probe experiments on Phthalic acid monomethylester (PMME) evinced coupling of the OH/OD stretching vibration to a low frequency mode which modulates the hydrogen bond length (cf. Section 1.2 and Fig. 1.2). The observed quantum beats reflect the anharmonic coupling between the two modes (see Fig. 1.1), since the excitation of the OH stretching vibration is accompanied by vibrational transitions with respect to the low frequency mode, giving rise to the oscillatory signal. Moreover, fast relaxation of the investigated mode indicated coupling to other degrees of freedom, and the theoretical investigations were to throw light on the mechanisms of relaxation processes.

The theoretical study of the relaxation of the OH stretching vibration of HOD in liquid D_2O [89], [90] suggested that the relaxation in this system takes place via the OH bending overtone, and the pathway to the ground state includes not just the intramolecular, but also the solvent modes. This proved that the investigated process is multidimensional, i.e., the coupling to other molecular modes is responsible for the fast energy flow from the OH stretching mode.

Recent experiments by Heyne et al. [91] on PMME provided more understanding of the deexcitation processes. They also observed oscillatory signal, Fig. 3.1 (a), which confirms intramolecular interactions. In a two - color experiment, the pump pulse excited the OH stretching vibration and the probe pulse was tuned in resonance with the OH bending mode, for instance. Those measurements proved that the relaxation of the stretching mode occurs via the bending fundamental vibration. In this section, we propose a mechanism for this process. Specifically, the relaxation pathway for this intramolecular hydrogen bond is shown to be different from the one which dominates the relaxation within the intermolecular hydrogen bond network in water.

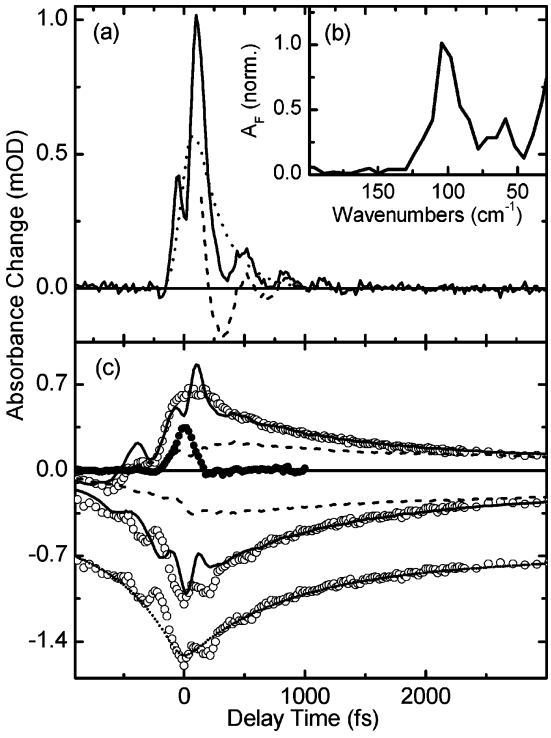

Figure 3.1: (a) Time dependent change of the OH stretch absorbance. (b) Normalized Fourier intensity of the oscillatory signal. (c) Transients of the OH bending absorbance after excitations of the OH stretching, CO stretching and OH bending vibrations. Taken from reference [91].

3.1 PMME - a System with a Medium Strong Hydrogen Bond

The molecule we will focus on in this chapter is Phthalic acid monomethylester, shown in Fig. 3.2. It contains a homonuclear medium-strong hydrogen bond. The dynamics of the deuterated species, PMME-D, has already been studied in the gas [92] and in the condensed phase [93], [94]. In the later case, a 3D relevant system model was employed for clarifying the experimental data. It comprised the OD stretching vibration ν_s, the OD out of plane bending vibration ν_b and the low frequency hydrogen bond mode ν_{low}. Additionally, two normal mode vibrations form the intramolecular bath which, together with the solvent modes (external bath), enable relaxation of the stretching mode. The fast relaxation was explained with a fourth order process that involves energy transfer from the ν_s vibration to two internal and one external bath mode. It is important to emphasize that the suggested model was not backed by experimental observations of the relaxation path. Such data became available only recently, but for the protonated species. However, although three significant degrees of freedom were sufficient for describing the PMME-D dynamics, the protonated species (PMME-H) is characterized by a different spectrum, and other modes are likely to be important for the hydrogen dynamics. Since the energy levels of PMME-H are shifted upwards compared to PMME-D, more normal modes can be combined to form Fermi res-

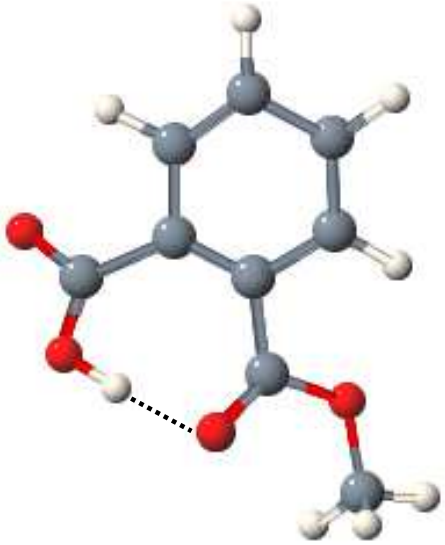

Figure 3.2: PMME molecule. The hydrogen bond is indicated with the dashed line.

onances with the OH stretching vibration. As will be shown in the following, five degrees of freedom were needed for an adequate description of the hydrogen bond dynamics in PMME-H.

As already mentioned, it was experimentally observed that the relaxation of the OH stretching vibration proceeds mainly via the OH bending mode. In addition, an oscillatory signal testified that the low frequency mode couples to the OH stretching vibration, giving rise to this signal. The low frequency mode actually modifies the distance between the donor and the acceptor and influences the hydrogen motion. In this section we will propose a mechanism for the relaxation of the OH stretching vibration, which includes the OH bending and the low frequency mode. Although the size of the molecule suggests that this is probably not the only relaxation chanel, according to the experimental results it is the most important one.

AFF Method - Numerical Results

First, the molecular structure has been optimized with the B3LYP exchange correlation functional and a 6-31+G(d,p) basis set, and the PES was constructed for the vicinity of this stationary point. Since we want to study the dynamics of the OH stretching vibration and this is a process that does not include large amplitude motion of any atom, the Anharmonic Force Field approach as detailed in Section 2.2.1 should provide a good description. The quality of the calculated anharmonic force fields with the B3LYP functional and a 6-31+G(d,p) basis set is discussed in Appendix C.

Having chosen the procedure for generating the PES, we continue by calculating the anharmonic force fields in order to select the relevant normal modes. Following the previous discussion, the cubic and quartic anharmonic terms are calculated according to Eq. 2.47 and 2.50, respectively. Since the force fields have relatively small values comparing to the quadratic terms, it is desirable to obtain them with high precision. The precision of the calculated anharmonic terms depends on [47]:

(i) the accuracy of the optimized reference (in our case equilibrium) structure;

(ii) the accuracy of the second derivatives of the potential;

(iii) the step size of the displacement along normal modes.

The requirements in items (i) and (ii) are taken care of by employing an *ultrafine grid*. Namely, the integrals given in Section 2.1.2 are solved numerically, so the precision of the calculations depends on the number of grid points (for further information about the number of grid points see Reference [95]).

Concerning the optimal step size, it depends on the accuracy of the second derivatives [47]: *"For a given relative error ϵ of the second derivatives, there is an optimum step size $\Delta\tilde{Q}$ for the finite difference procedure such that the numerical errors due to ϵ (which decrease with increasing $\Delta\tilde{Q}$) are equal to the truncation errors due to the neglect of the higher derivatives (which increase with increasing $\Delta\tilde{Q}$)"*. In order to find an optimal displacement for our system, we performed a series of calculations for different displacements, Fig. 3.4. Panels (A) and (B) correspond to cubic terms k_{bbb} (for the bending mode ν_b, Fig. 3.3 right) and k_{sss} (for the stretching mode ν_s Fig. 3.3 left), which are calculated according to Eq. 2.47. Comparing those two graphs, we see that the larger the numerical value of the anharmonic term, the smaller is the influence of the step size. For the step sizes 0.030, 0.040 and 0.050 (in dimensionless normal mode coordinates), the difference is approximately 1.5/2 cm^{-1} for the bending/stretching mode which corresponds to the relative error of about 1/0.07 %. Focusing on the bending mode, the plot suggests the step size between 0.030 and 0.040 to be optimal due to the change of the trend - probably for lower and higher values, the errors accumulate, leading to lower values of this term. That is also the case for the stretching mode, but one should keep in mind that the relative error for this case is rather small, so for high frequency modes it does not introduce significant errors. Panels (C) and (D) stand for the mixed terms k_{bbs} and k_{bss}. They describe the modification of the bending mode due to its interaction with the stretching mode and vice versa. The

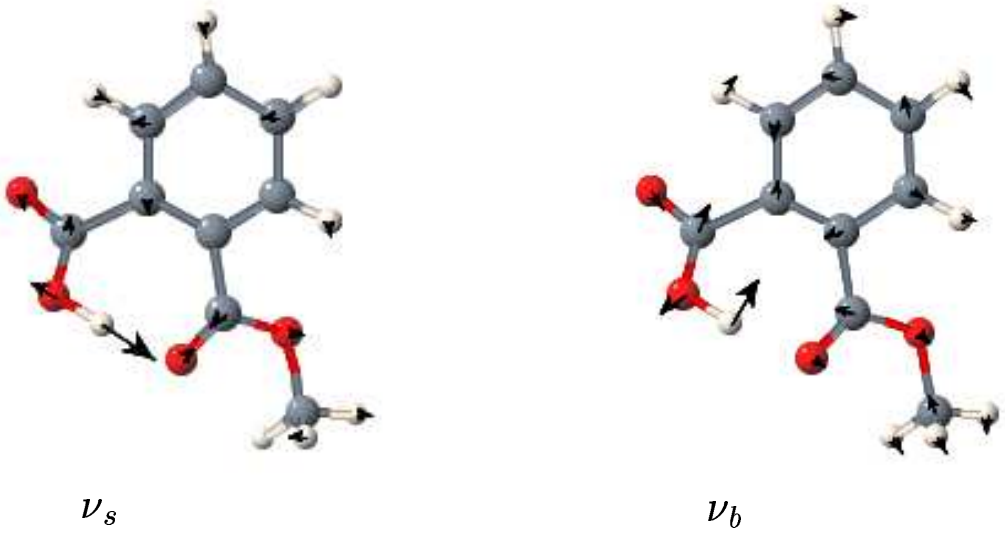

Figure 3.3: The OH stretching, ν_s, and the OH bending, ν_b, mode in PMME.

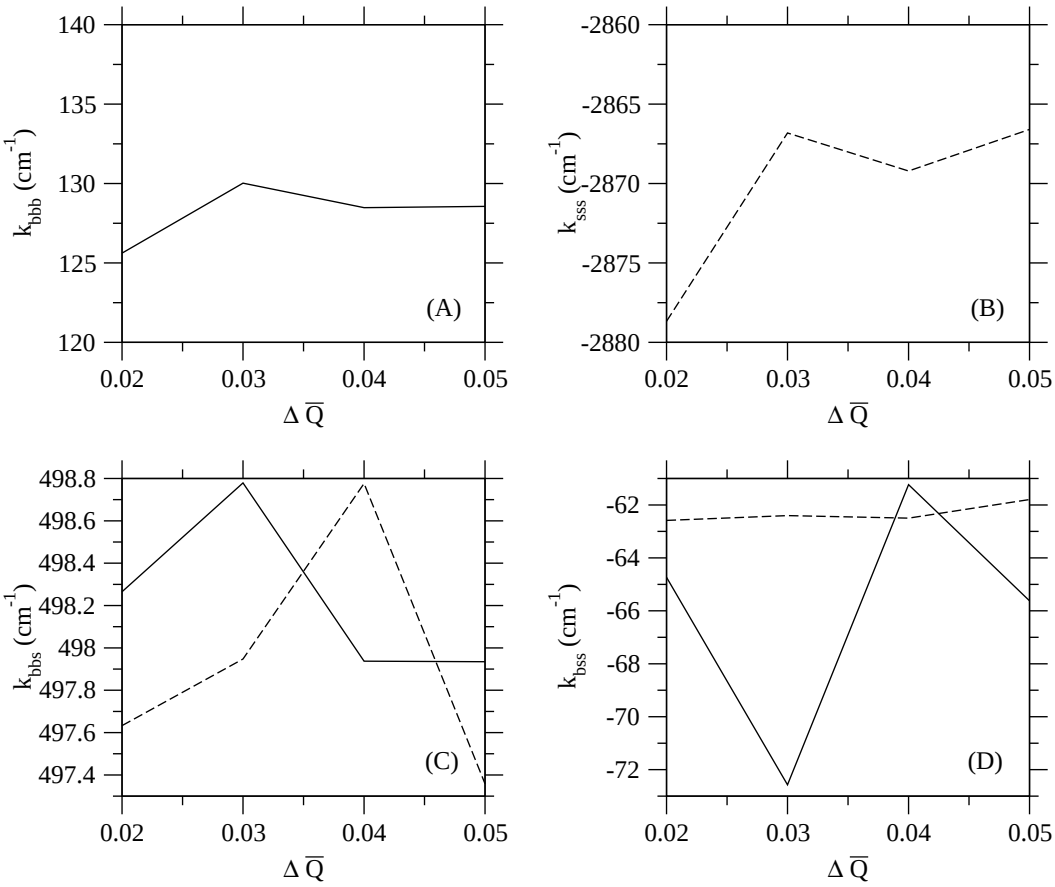

Figure 3.4: Finding the optimal displacement for the calculation of the cubic force fields for the (A) OH bending (b) and (B) OH stretching (s) vibration, as well as the mixed terms (C) k_{bbs} and (D) k_{bss}. $\Delta\tilde{Q}$ is the dimensionless normal mode coordinate. On panels (C) and (D), the solid and the dashed lines correspond to the displacements along the bending and the stretching mode respectively.

former term has a value which is an order of magnitude higher than the latter due to the Fermi resonance (the overtone of the bending mode lies close in resonance to the fundamental stretching transition). Another interesting feature of k_{bss} is that the calculation reveals a better convergence if the displacement is performed along the stretching mode (dashed line) since the anharmonicity of the potential along the stretching mode is more pronounced comparing to the one of the bending mode (cf. Panels (A) and (B)).

As to the quartic force fields, the results are displayed in Fig. 3.5. Concerning the diagonal bending k_{bbbb} and stretching k_{ssss} terms, Panels (A) and (B), we follow the same reasoning as for the cubic terms and conclude that the displacement 0.040 is the optimal one. The relative accuracy for the OH stretching mode is 2 % (for this comparison the result that correspond to $\Delta\tilde{Q} = 0.020$ are not taken into account). Concerning the k_{bbbb} term, low accuracy 20 %, suggests that the dis-

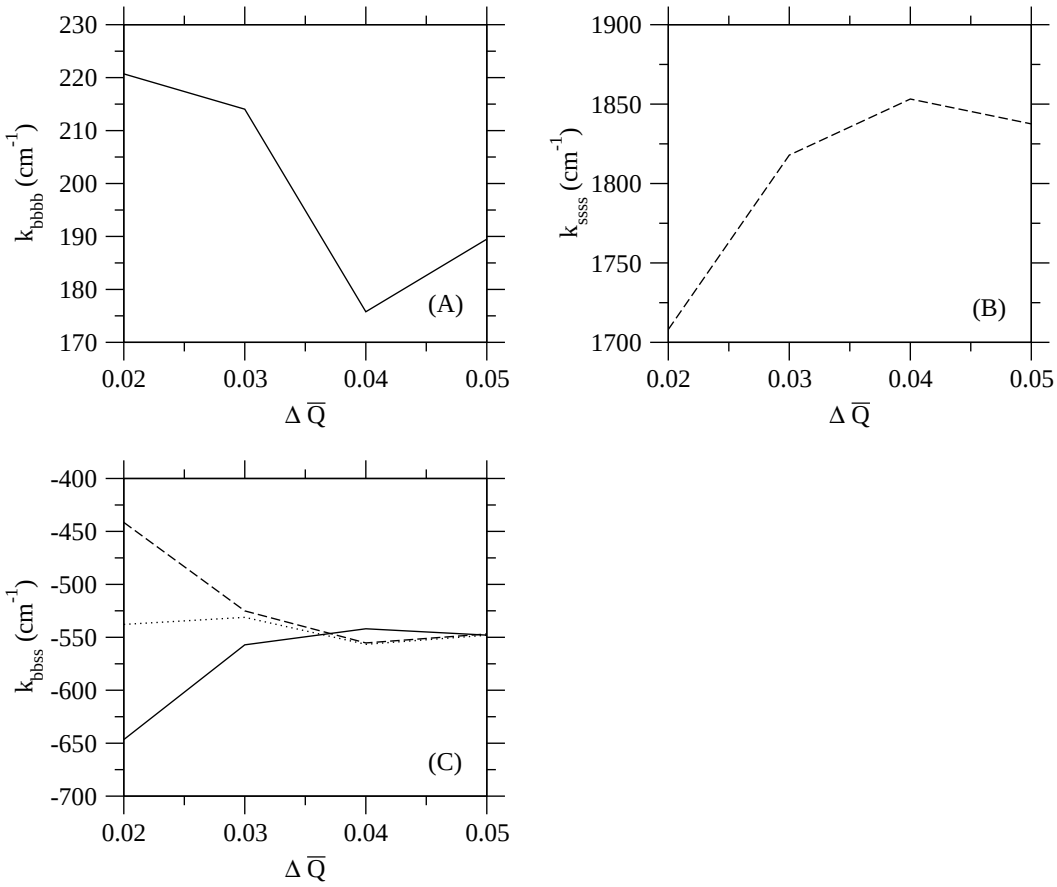

Figure 3.5: Calculation of the quartic force fields: (A) k_{bbbb}; (B) k_{ssss}; (C) k_{bbss}. The solid, dashed and dotted line correspond to the displacements along the bending mode, the stretching mode, and simultaneously along the bending and the stretching mode, respectively.

placement $\Delta\tilde{Q} = 0.030$ is not appropriate for calculating the quartic terms, since the errors accumulate and lead to unreliable results. Again, the trend for the high frequency term is more obvious. Concerning the mixed term k_{bbss}, Panel (C), we note again that the accuracy of the calculated term is higher if the displacement is performed along the "more anharmonic" mode.

To summarize, for our calculations we used the displacement 0.030/0.040 for the calculation of the cubic/quartic anharmonic terms according to Eq. 2.47/2.50. In addition, it will be shown in the following that the couplings between most strongly coupled modes have been treated exactly, i.e., by calculating the potential on a grid, since according to the values of the calculated force fields, the interaction between those modes is rather strong and probably would not be described properly by two lowest anharmonic terms.

Selection of Relevant Degrees of Freedom

Our goal is to model the relaxation of the OH stretching vibration, ν_s. Before we turn to a specific system, let us consider a general *Tier model*, Fig. 3.6. After an excitation of the bright state, the energy is transferred to the neighboring states (that form the 1$^{\text{st}}$ tier) to which it is coupled. Those states are coupled to the next manifold of states (2$^{\text{nd}}$ tier) and so on. The larger the system, the more complicated its Tier model is.

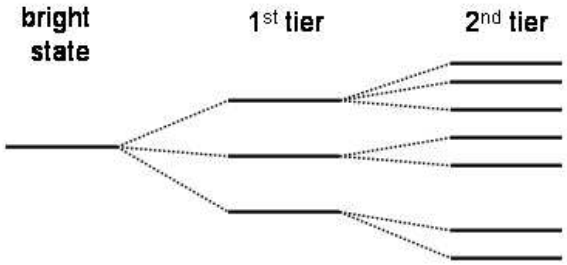

Figure 3.6: The Tier model. After the excitation of the bright state, the energy is transferred to the states forming the first tier, then further to the second tier, etc.

Turning back to our system, the bright state represents the ν_s mode and the first task is to recognize the modes that form the 1$^{\text{st}}$ tier, i.e., the most strongly coupled modes. It is known from the experiment that the OH bending mode, ν_b, and a certain low frequency mode, ν_{low} with a frequency around 100 cm^{-1}, take part in the vibrational dynamics of ν_s. The next step is to identify this low frequency mode, and in addition further degrees of freedom that couple to the hydrogen motion on the basis of the quantum chemical calculations. Modes ν_s and ν_b are shown in Fig. 3.3. Concerning the low frequency mode, there are two possibilities, Fig. 3.7. The harmonic values of the frequencies of ν_{low} and $\nu_{low'}$ are 39 cm^{-1} and 72 cm^{-1}, respectively. However, the anharmonic terms that correspond to $k_{s,s,low}$ and $k_{s,s,low'}$ are -73 cm^{-1} and 8 cm^{-1}, and for $k_{b,b,low}$ and $k_{b,b,low'}$, 15 cm^{-1} and -5 cm^{-1}, respectively. In other words, mode ν_{low} has much stronger influence on the OH stretching and the OH bending mode than $\nu_{low'}$. Additionally, the anharmonic value ω_{low}^{anh} is 65 cm^{-1} (calculated from the uncoupled one-dimensional potential) which leads to a conclusion that the experimentally observed mode is more likely to be identified with ν_{low}.

Having identified ν_s, ν_b and ν_{low}, we checked how well the AFF procedure reproduces the 1D potentials along those modes. The potentials that correspond to the OH stretching and bending vibration are depicted on Fig. 3.8. The solid lines

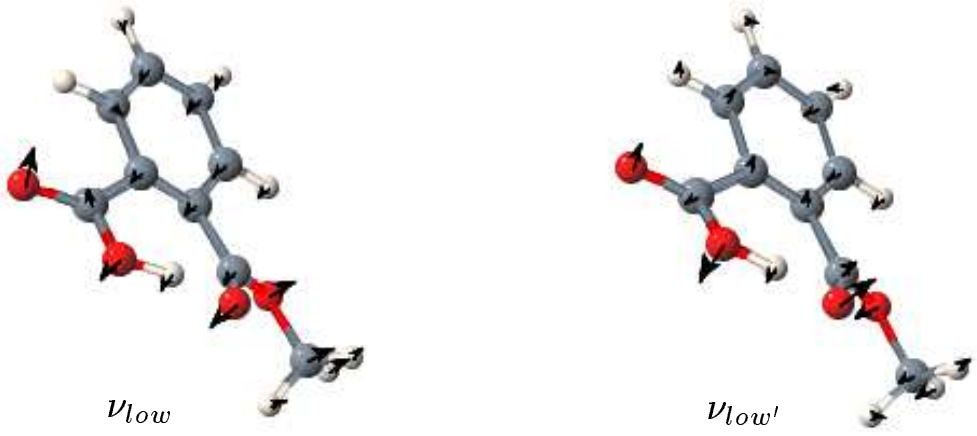

Figure 3.7: The two candidates for the low frequency mode.

stay for the potentials obtained on a grid by displacing the structure along the corresponding mode. The dashed lines are obtained from the AFF approach, i.e.,

$$V^{(1)}(Q_i) = V_{eq} + \frac{1}{2}K_{i,i}Q_i^2 + \frac{1}{6}k_{i,i,i}Q_i^3 + \frac{1}{24}k_{i,i,i,i}Q_i^4. \tag{3.1}$$

The potential energy curve (PEC) for ν_s is shown on Panel (A). Close to the equilibrium, Eq. 3.1 represents a good approximation to the true potential. However,

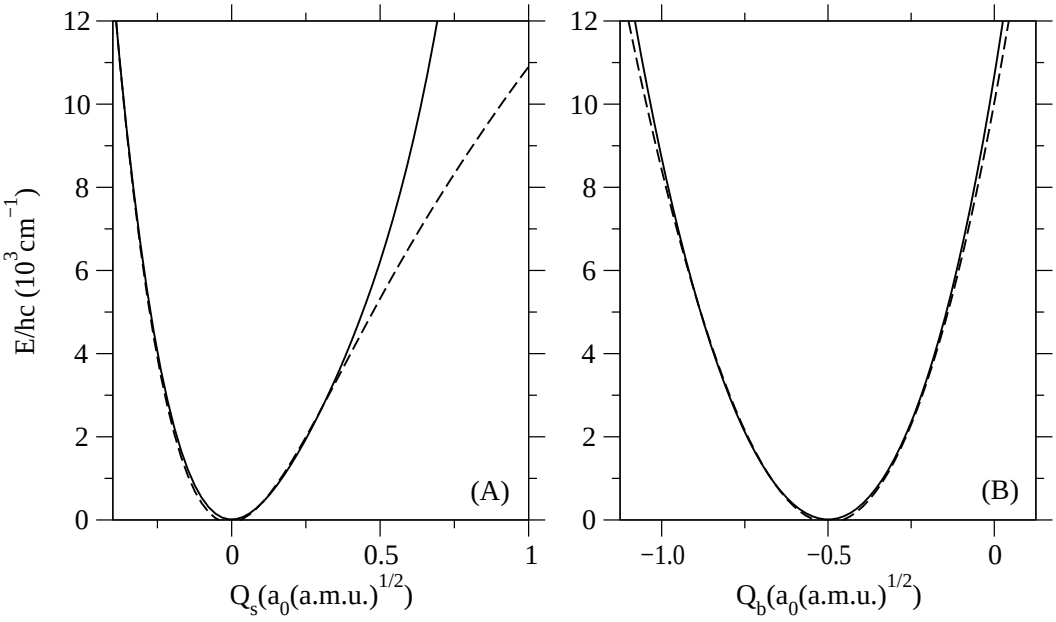

Figure 3.8: One - dimensional potentials along ν_s and ν_b. The solid lines represent potentials on a grid, and the dashed curves correspond to Eq. 3.1.

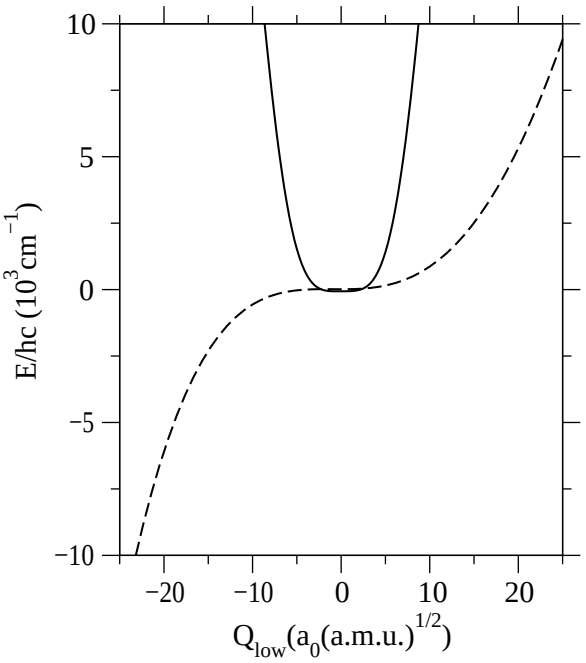

Figure 3.9: One - dimensional potentials along ν_{low}. The solid/dashed line represent potentials on a grid/Eq. 3.1.

for large displacements the two curves start to diverge. Concerning ν_b, the anharmonicity of this mode is not very pronounced, so the model potential can describe the system well even above 10^4 cm^{-1}.

The situation is quite different for ν_{low}, Fig. 3.9. The potential on a grid resembles a square well potential. Its anharmonicity can not be described with the two lowest anharmonic terms, even for very small displacements. That is, one would have to compute higher order derivatives of the potential in order to obtain reasonable results.

The next step is to examine the force fields that involve the above three modes to find out which of the remaining intramolecular modes are strongly coupled. By analyzing the cubic and the quartic anharmonic terms, we identified two normal modes, γ_1 and γ_2, shown on Fig. 3.10 that couple to the above mentioned degrees of freedom, in particular to ν_b. They have an OH out of plane bending character. The harmonic and the anharmonic frequencies (computed from $V^{(1)}(Q_i)$) are given in Table 3.1, which confirm the marked anharmonicity along ν_s and ν_{low}. Notice that the selection was also based on energetic arguments, a point which will be explained in more detail below.

Some of the cubic and the quartic anharmonic terms are compiled in Tables 3.2 and 3.3, respectively.

Having chosen the relevant degrees of freedom, we proceed by calculating the potential energy surface. It would be desirable to generate a potential on a 5D grid.

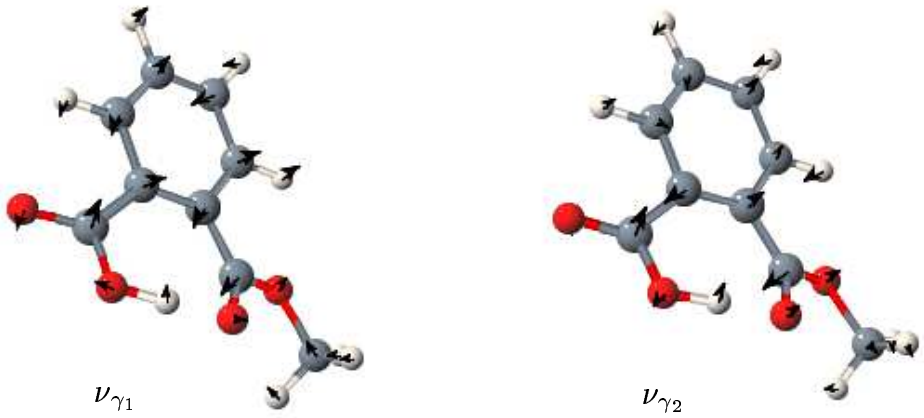

Figure 3.10: The two additional normal mode vibrations of PMME, ν_{γ_1} and ν_{γ_2}.

i	ν_s	ν_b	ν_{low}	ν_{γ_1}	ν_{γ_2}
ω_i^h (cm^{-1})	3279	1446	39	682	785
ω_i^{anh} (cm^{-1})	3005	1485	65	685	788

Table 3.1: Normal mode vibrations of PMME: ω_i^h and ω_i^{anh} correspond to harmonic and anharmonic values respectively.

i,j,k	$k_{i,j,k}$ in cm^{-1}
s,s,s	-2867
s,b,b	498
b,b,b	130
s,low,low	94
b,low,low	-93
s,γ_2,γ_2	76
s,s,low	-73
s,low,γ_2	-70
s,s,b	-62
s,s,γ_2	50
s,s,γ_1	46
s,γ_1,γ_2	43

i,j,k	$k_{i,j,k}$ in cm^{-1}
s,low,γ_1	-36
b,low,γ_2	35
b,low,γ_1	26
s,γ_1,γ_1	23
low,low,low	-20
s,b,γ_1	-16
b,b,low	15
low,γ_1,γ_1	-13
s,b,γ_2	-13
low,low,γ_1	-12
b,γ_1,γ_2	11
b,γ_2,γ_2	9

Table 3.2: Significant cubic anharmonic terms that involve ν_b, ν_s and ν_{low}.

However, that would require appreciable computational costs, so we are forced to find an appropriate approximation to the exact five - dimensional hypersurface.

i,j,k,l	$k_{i,j,k,l}$ in cm^{-1}
s,s,s,s	1853
s,s,b,b	-555
low,low,low,low	384
s,s,low,low	-275
b,b,b,b	176
s,s,low,γ_2	100
s,s,s,b	83
s,s,γ_2,γ_2	-80
s,s,low,γ_1	74
s,b,b,b	-73
low,low,low,γ_2	-51
s,s,b,low	50
s,s,γ_2,γ_1	-47
s,s,γ_1,γ_1	-35
s,s,s,γ_2	-31

i,j,k,l	$k_{i,j,k,l}$ in cm^{-1}
s,s,s,γ_1	-31
$low,low,\gamma_2,\gamma_2$	30
b,b,low,low	-30
b,b,low,γ_2	-25
low,low,low,γ_1	-24
b,low,low,low	22
s,b,low,low	22
$low,low,\gamma_1,\gamma_2$	21
s,s,s,low	20
$low,low,\gamma_1,\gamma_1$	18
b,b,b,γ_1	-16
b,b,low,γ_1	14
b,b,b,low	14
b,b,γ_1,γ_1	-13
b,b,b,γ_2	-12

Table 3.3: Significant quartic anharmonic terms that involve ν_b, ν_s and ν_{low}.

Consider the following expression for the potential (cf. Eq. 2.37)

$$V(\mathbf{Q}) = \sum_n V^{(n)}(\mathbf{Q}) = \sum_i V^{(1)}(Q_i) + V^c(\mathbf{Q}) \tag{3.2}$$

where $\mathbf{Q}$ comprises all five degrees of freedom. $V^{(1)}(Q_i)$ stands for the potentials of the uncoupled modes, whereas $V^c(\mathbf{Q})$ describes the couplings between them. The 1D potentials are easily obtainable. For the 2 - mode coupling potentials, we decided to calculate them explicitly on the grid for those pairs of modes which are most strongly coupled (i.e., ν_s, ν_b and ν_{low}). Such a treatment has been suggested by our attempt to obtain a converged force field (cf. Fig. 3.4 (D), for instance). All other 2 - mode couplings as well as 3 - mode and 4 - mode couplings are included via anharmonic force field terms. Hence, the total potential is given by

$$\begin{aligned} V(\mathbf{Q}) &= \sum_i V^{(1)}(Q_i) + (V(Q_s,Q_b) + V(Q_s,Q_{low}) + V(Q_b,Q_{low})) + \\ &\quad \frac{1}{3!}\sum_{ijk} k_{ijk}Q_iQ_jQ_k + \frac{1}{4!}\sum_{ijkl} k_{ijkl}Q_iQ_jQ_kQ_l \end{aligned} \tag{3.3}$$

Note that the last two sums do not include terms which are already given by 2D potentials ($k_{s,b,b}$, for instance).

In order to investigate the dynamics of the relevant system, the 5 - dimensional Hamiltonian needs to be diagonalized. To this end we start by defining a

basis of uncoupled anharmonic modes $\{|\phi_n^{\nu_i}\rangle\}$, which are obtained by solving the Schrödinger equation

$$H_i|\phi_n^{\nu_i}\rangle = \left[T_i + V^{(1)}(Q_i)\right]|\phi_n^{\nu_i}\rangle = E_n^{\nu_i}|\phi_n^{\nu_i}\rangle \tag{3.4}$$

with the Fourier grid Hamiltonian method ([96]). Since the vibrational period of the low frequency mode is much longer than for the other four modes, it will be convenient to introduce a diabatic representation with respect to ν_{low}, i.e., a time independent Schrödinger equation is solved

$$\left[\sum_i H_i + V^{(c)}(\mathbf{Q}_{fast}, Q_{low} = 0)\right]|\alpha\rangle = E_\alpha|\alpha\rangle. \tag{3.5}$$

level	E (cm^{-1})	(v_s,v_b,v_{γ_1},v_{γ_2})	$C_{\alpha,ijkl}$
1	0	(0,0,0,0)	1.000
2	693	(0,0,0,1)	0.997
3	799	(0,0,1,0)	0.997
4	1385	(0,0,0,2)	0.995
5	1455	(0,1,0,0)	-0.991
6	1501	(0,0,1,1)	-0.988
7	1601	(0,0,2,0)	-0.994
8	2077	(0,0,0,3)	-0.992
9	2149	(0,1,0,1)	-0.987
10	2202	(0,0,1,2)	0.980
11	2253	(0,1,1,0)	0.988
12	2312	(0,0,2,1)	0.977
13	2406	(0,0,3,0)	0.987
15	2841	(0,1,0,2)	-0.945
16	2853	(0,2,0,0)	-0.817
		(1,0,0,0)	0.486
18	2956	(0,1,1,1)	-0.976
19	3022	(0,0,2,2)	-0.960
20	3044	(1,0,0,0)	-0.837
		(0,2,0,0)	-0.492
21	3054	(0,1,2,0)	-0.962

Table 3.4: Energies of the selected diabatic states and assignment, expressed in terms of the uncoupled anharmonic modes. The last column contains relevant expansion coefficients.

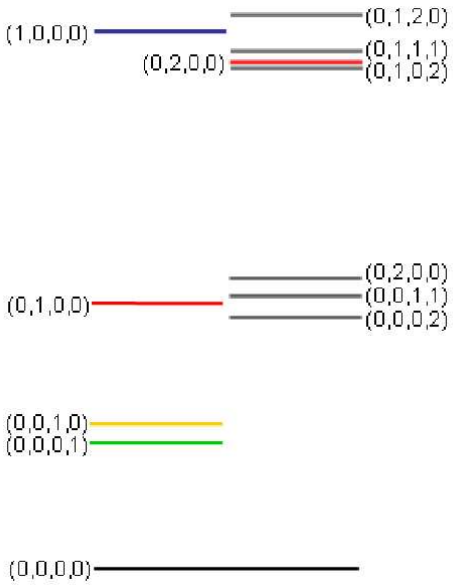

Figure 3.11: Energy levels of the diabatic states. The lines on the left stand for the fundamental transitions of the fast modes: green - ν_{γ_1}, yellow - ν_{γ_2}, red - ν_b, blue - ν_s. The levels on the right side represent overtone and combination transitions.

with $\mathbf{Q}_{fast} = \{Q_s, Q_b, Q_{\gamma_1}, Q_{\gamma_2}\}$ and the first sum runs over the *fast* modes. The zero - order states $\{|\alpha\rangle\}$ are further expanded in a basis of uncoupled anharmonic modes

$$|\alpha\rangle = \sum_{ijkl} C_{\alpha,ijkl} |\phi_i^{\nu_s}\rangle |\phi_j^{\nu_b}\rangle |\phi_k^{\nu_{\gamma_1}}\rangle |\phi_l^{\nu_{\gamma_2}}\rangle \tag{3.6}$$

The leading configurations are compiled in Table 3.4. Note the presence of Fermi resonance: $|\alpha = 16\rangle$ and $|\alpha = 20\rangle$ represent mixed states, although the former corresponds dominantly to the bending overtone and the latter to the stretching fundamental transition. Such strong interaction justifies an exact treatment of the coupling between those two modes.

Some of the diabatic levels are shown in Fig. 3.11. The fundamental transitions of the fast four modes are depicted on the left side. The overtone and the combination transitions of the two out of plane bending modes lie close in resonance to the ν_b transition. On the other side, the first overtone of ν_b, as well as the combination of ν_b and the overtones of ν_{γ_1} and ν_{γ_2} form the stretching band. These resonance conditions have also been the guide for including the two additional modes into our model. The scheme depicted in Fig. 3.11 already suggests possible relaxation channels of the OH stretching and bending mode.

After defining the diabatic states, the total Hamiltonian in the diabatic repres-

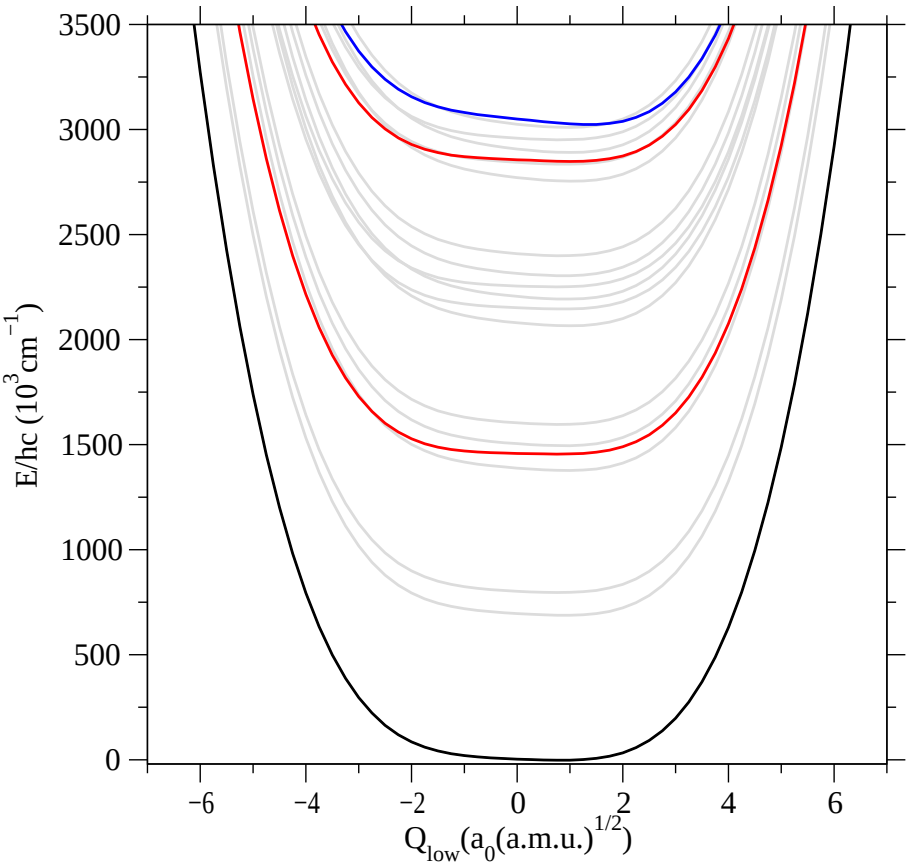

Figure 3.12: The diabatic potential energy curves. The black line corresponds to the ground state, the lower red line stands for the state that has dominantly OH in plane bending character, whereas the upper red curve represents its overtone. The state marked with the blue color has mainly OH stretching character.

entation is given by

$$H^{diab} = \sum_{\alpha\beta} \left[\delta_{\alpha\beta}\left(T_{low} + E_\alpha + V_{\alpha\alpha}(Q_{low})\right) + \left(1-\delta_{\alpha\beta}\right) V_{\alpha\beta}(Q_{low})\right] |\alpha\rangle\langle\beta| \tag{3.7}$$

with

$$V_{\alpha\beta}(Q_{low}) = \langle\alpha|V^{(1)}(Q_{low}) + V^c(\mathbf{Q}_{fast}, Q_{low}) - V^c(\mathbf{Q}_{fast}, Q_{low}=0)|\beta\rangle. \tag{3.8}$$

being responsible for the population transfer since it represents the coupling between the diabatic levels. $V^c(\mathbf{Q}_{fast}, Q_{low})$ accounts for the coupling between the four *fast* modes with the low frequency mode.

The diabatic potential energy curves, $V_{\alpha\alpha}(Q_{low})$, are shown in Fig. 3.12. Recall that each of the diabatic curves contains vibrational levels with respect to the low frequency mode. In addition, the anharmonic value of ν_{low} is only $65\ \mathrm{cm}^{-1}$ (cf. Table 3.1), so by climbing along the energy scale, the density of states increases

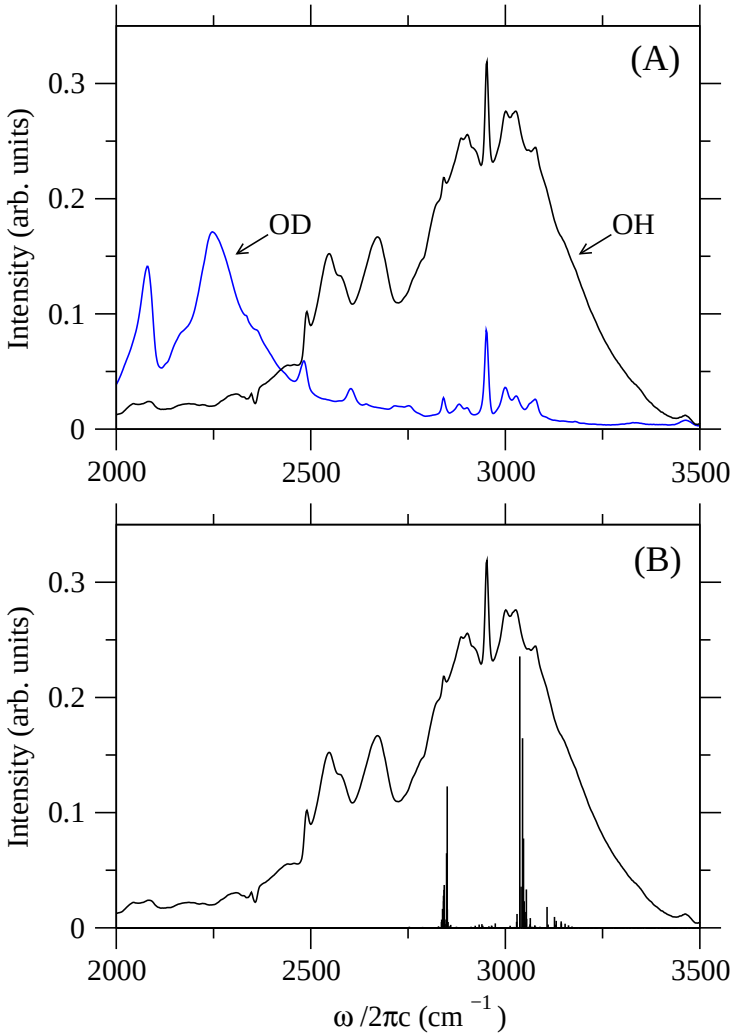

Figure 3.13: (A) Experimental spectra for PMME-H (black) and PMME-D (blue line) (courtesy of K. Heyne). The arrows point at the OD and the OH stretching band. (B) Experimental spectrum for PMME-H and the calculated stick spectrum.

considerably. The black line represents the ground state, the first red line the fundamental ν_b transition, and the next red line its overtone. The blue line stands for the state that has dominantly OH stretching character.

Further, we calculated the stick spectrum according to

$$I(\omega) = \sum_{\alpha\beta} P_\alpha \left| d_{\alpha\beta} \right|^2 \delta(\omega - \omega_{\beta\alpha}) \tag{3.9}$$

with P_α being the distribution function and $d_{\alpha\beta}$ the transition dipole moment. The results are shown in Fig. 3.13, Panel (B), together with the experimental spectrum. The experimental spectra of the protonated and the deuterated species are given in Panel (A), with marked bands that correspond to the OH and OD stretching transitions. The broad band between 2750 and 3250 cm^{-1} corresponds to transitions

that include the highest manifold of states depicted in Fig. 3.12. The interaction of the bending overtone and the stretching mode is responsible for the appearance of the double peak structure, which can be clearly seen in the stick spectrum as well.

The model for the relevant system is now completely defined. Before proceeding to the dynamics, we will discuss the interaction with the surrounding.

3.1.1 System - Bath Coupling

In order to model the fast relaxation of the ν_s mode which was observed in the experiment, we included two types of interaction with the bath, bilinear coupling and third order coupling.

Bilinear coupling. If Eq. 2.109 is understood as Taylor expansion of the PES, it is to be expected that the lowest order terms have the greatest significance. Therefore, in order to study the interaction between the relevant system and the solvent, we will consider first the lowest order term, i.e., linear term with respect to the system $\{\tilde{\mathbf{Q}}\}$ and reservoir $\{\tilde{\mathbf{Z}}\}$ (external bath) degrees of freedom

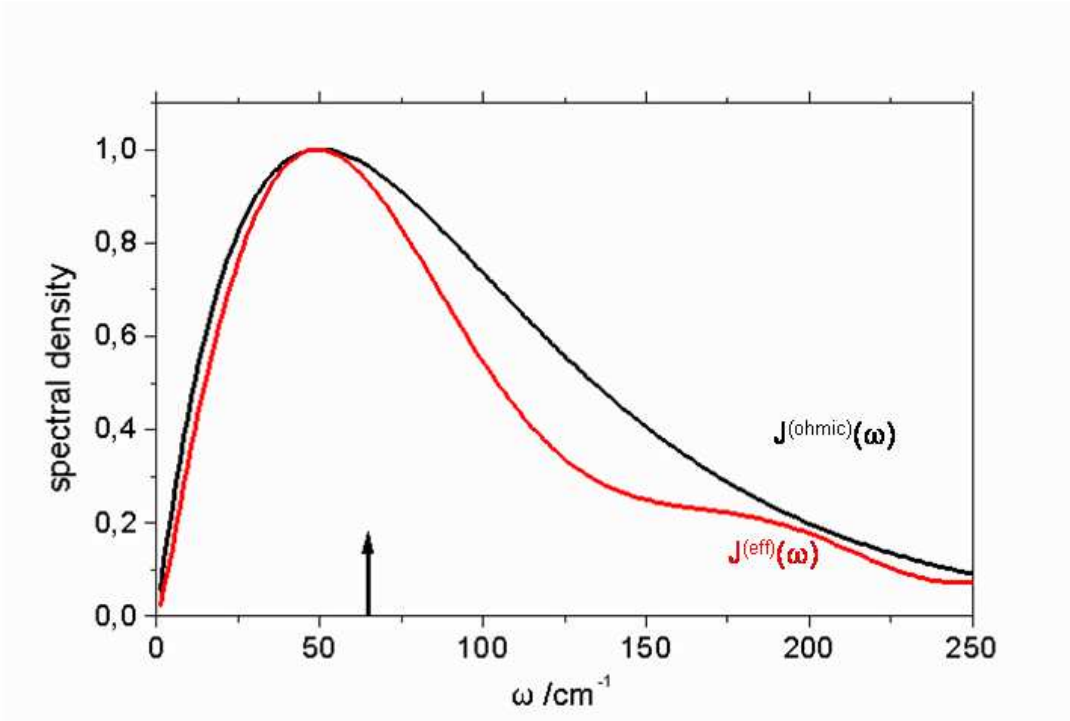

Figure 3.14: Red line: spectral density obtained from the MD simulations. Black line: ohmic spectral density. The arrow indicates ω_{low}^{anh} (taken from Ref. [94]).

$$\hat{H}_{SR}^{(I)} = \tilde{Q}_{low} \sum_{\lambda} \hbar\omega_\lambda g_\lambda^{(I)} \tilde{Z}_\lambda \tag{3.10}$$

where g_λ represents the coupling constant for the bath oscillator with frequency ω_λ. This quantity was obtained from classical molecular dynamics simulations of PMME in CCl_4 at 300 K (performed by H. Naundorf [65]). The spectral density, calculated according to Eq. 2.128, is displayed in Fig. 3.14 with the red line, $J^{(\mathrm{eff})}(\omega)$, and was approximated by the ohmic spectral density $J^{(\mathrm{ohmic})}(\omega)$ [67]

$$J^{(\mathrm{ohmic})}(\omega) = J^{(I)}(\omega) = |g^{(I)}|^2 \Theta(\omega)\omega e^{-\omega/\omega_c} \tag{3.11}$$

where ω_c stands for the cut-off frequency. The step function $\Theta(\omega)$ insures that the spectral density is equal to zero for negative frequencies. The arrow in Fig. 3.14 indicates the anharmonic value of ν_{low}. It almost coincides with the maximum of the spectral density, which means that the transfer of energy from this mode to the solvent should be efficient. Starting from this expression the bath correlation function obtains the form

$$C_{low}^{(I)}(\omega) = \pi(1 + n(\omega))[J^{(I)}(\omega) - J^{(I)}(-\omega)] \tag{3.12}$$

where $n(\omega)$ stands for the Bose-Einstein distribution function for the reservoir modes.

Third order coupling. The linear coupling discussed above describes relaxation of the ν_{low} mode. However, the other four modes have rather high frequencies and cannot directly transfer the energy to the solvent. Therefore, it is necessary to find another channel for their relaxation.

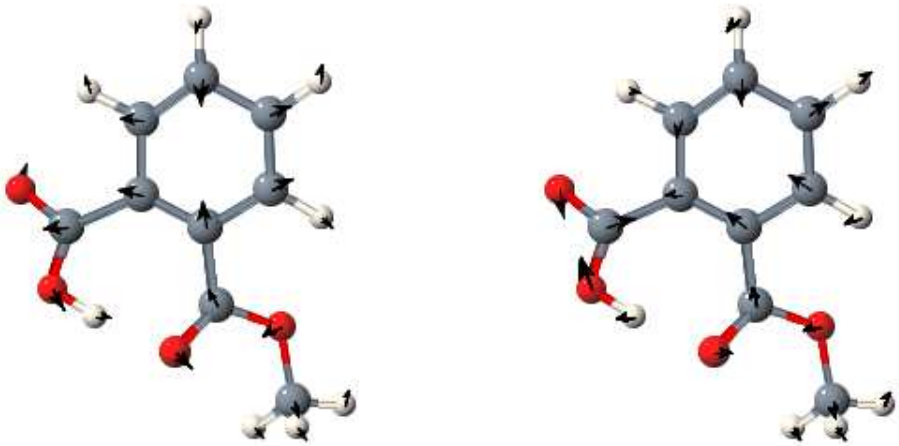

ν_{b_1} ν_{b_2}

Figure 3.15: Modes ν_{b_1} and ν_{b_2} with frequencies 694 cm^{-1} and 795 cm^{-1} form the intramolecular bath.

Recall the Tier model which was introduced when selection of modes that form the relevant system was discussed. The first tier for ν_s and ν_b is easily recognizable from Fig.3.11, which suggests that the ν_s mode might relax by transferring the energy to the other four modes, while ν_b is coupled to three close lying levels corresponding to the overtone and combination transitions of ν_{γ_1} and ν_{γ_2}. That is, the energy ends up in the three modes having the lowest energy. In principle, one could proceed further, and according to the calculated force fields identify other molecular modes that can accept the excess of energy from the two out of plane bending modes. However, including additional modes into the relevant system would result in a model of a rather high dimensionality, which would lead to a drastic increase of the CPU time. Therefore, we included two additional modes of the PMME molecule, Fig. 3.15, ν_{b_1} and ν_{b_2} that form the *internal bath* and to which, according to the calculated force fields, the energy should be efficiently transferred. Those two modes are close in energy to ν_{γ_1} and ν_{γ_2}, and the energy gap is bridged by the solvent modes, as shown in Fig. 3.16. This 3$^{\text{rd}}$ order coupling is given by

$$\hat{H}_{SR}^{(II)} = \tilde{Q}_{\gamma_1} \sum_{\lambda} \hbar\omega_\lambda g_{\gamma_1,b_1,\lambda}^{(II)} \tilde{q}_{b_1} \tilde{Z}_\lambda + \tilde{Q}_{\gamma_2} \sum_{\lambda} \hbar\omega_\lambda g_{\gamma_2,b_2,\lambda}^{(II)} \tilde{q}_{b_2} \tilde{Z}_\lambda \tag{3.13}$$

with $\{\tilde{q}_b\}$ being the coordinates of the internal bath modes. Notice that the solvent mode is also necessary because there would be no 2$^{\text{nd}}$ order coupling. Additionally, we will assume the same coupling strength between the pairs (ν_{γ_1}, ν_{b_1}) and (ν_{γ_2}, ν_{b_2}) which leaves us with a single parameter $g_{\gamma_1,b_1,\lambda}^{(II)} = g_{\gamma_2,b_2,\lambda}^{(II)} \to g^{(II)}$. The reservoir correlation function reads [67]

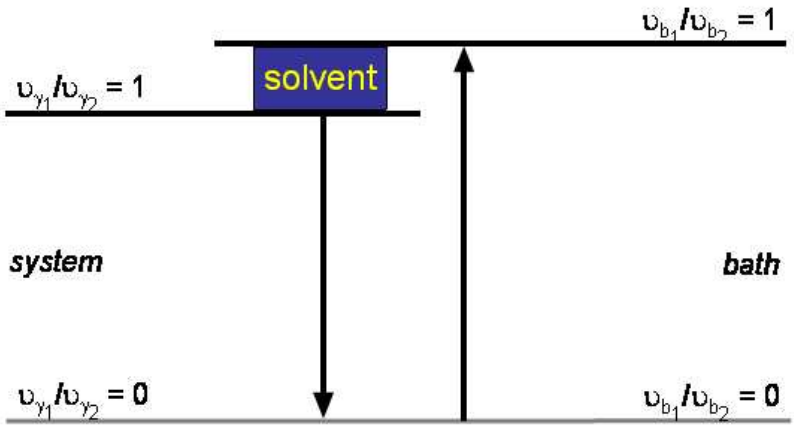

Figure 3.16: Coupling of the system degrees of freedom to the internal and the external bath, Eq. 3.13.

$$\begin{aligned} C_{ii}^{(II)}(\omega) &= \pi(1+n(\omega_{b_i}))(1+n(\omega-\omega_{b_i})) \\ &\quad [J^{(II)}(\omega-\omega_{b_i}) - J^{(II)}(-(\omega-\omega_{b_i}))] \\ &\quad +\pi n(\omega_{b_i})(1+n(\omega+\omega_{b_i})) \\ &\quad [J^{(II)}(\omega+\omega_{b_i}) - J^{(II)}(-(\omega+\omega_{b_i}))] \end{aligned} \tag{3.14}$$

with i = 1, 2. The off-diagonal terms $C_{ij}^{(III)}$ vanish, since for the harmonic oscillator bath $\langle q_{b_1}(t)Z_\lambda(t)q_{b_2}(0)Z_\lambda(0)\rangle = 0$.

It should be emphasized that this is not the only relaxation mechanism for ν_{γ_1} and ν_{γ_2}. For example, there is a mode with frequency 337 cm^{-1}, whose overtone is close in energy with the above two modes. However, the energy difference would have to be compensated with a bath mode, which would result in a 4$^{\text{th}}$ order process. Most likely, this mechanism would be less efficient than the one we consider.

To summarize, the total system - bath Hamiltonian reads

$$\hat{H}_{SR} = Q_{low}\sum_\lambda g_\lambda^{(I)} Z_\lambda + Q_{\gamma_1}\sum_\lambda \hbar\omega_\lambda g_{\gamma_1,b_1,\lambda}^{(II)} q_{b_1} Z_\lambda + Q_{\gamma_2}\sum_\lambda \hbar\omega_\lambda g_{\gamma_2,b_2,\lambda}^{(II)} q_{b_2} Z_\lambda \tag{3.15}$$

The first sum describes the relaxation of the low frequency mode, while the other two terms allow relaxation of the two out of plane bending modes. The coupling strength $g^{(I)}$ is obtained from MD simulation, and the only parameter that needs to be fitted in order to reproduce the experimentally observed IVR times for ν_s and ν_b is $g^{(II)}$, which stands for the coupling between the system and the internal bath. The internal bath consists of two normal modes, ν_{b_1} and ν_{b_2}, which are close in energy to ν_{γ_1} and ν_{γ_2}.

3.2 Population Dynamics of the Cascaded Energy Relaxation

In order to follow the system dynamics, we used the Redfield approach within the Bloch limit, Section 2.3.2. The propagation of the reduced density matrix is performed in the energy representation [67], i.e., the basis formed by the eigenstates of the total Hamiltonian (cf. Eq. 3.7) $\{|a\rangle\}$

$$H^{diab}|a\rangle = E_a|a\rangle. \tag{3.16}$$

For the purpose of following the populations of the zero-order states, the ei-

genstates of the full Hamiltonian are expanded in the basis of the diabatic states

$$|a\rangle = \sum_{\alpha,M_\alpha} C^a_{\alpha M_\alpha} |\alpha\rangle |\chi_{\alpha M_\alpha}\rangle \tag{3.17}$$

where $|\chi_{\alpha M_\alpha}\rangle$ correspond to ν_{low}, i.e., they are eigenstates of the uncoupled diabatic potential curves and C^a_{α,M_α} are the expansion coefficients. Hence, the relation between the density matrices in the eigenstate and the diabatic representation is given by

$$\rho_{ab} = \sum_{\alpha,M_\alpha} \sum_{\beta,M_\beta} C^a_{\alpha M_\alpha} \rho_{\alpha M_\alpha,\beta N_\beta} C^b_{\beta N_\beta} \tag{3.18}$$

We will consider a Frank-Condon like transition that corresponds to a vertical transition from the ground state to the state of interest (in our case those are the states that describe the OH bending and stretching motion). Neglecting the diabatic state couplings, the initial condition is given by [67]

$$\rho_{\alpha M_\alpha,\alpha N_\alpha}(t=0) = \langle \chi_{\alpha M_\alpha} | \chi_{00} \rangle \langle \chi_{00} | \chi_{\alpha N_\alpha} \rangle \tag{3.19}$$

where $|\chi_{00}\rangle$ stands for the ground state. The equation of motion of the density matrix (cf. Eq. 2.113 and 2.120) in the energy representation in the Bloch limit reads

$$\frac{\partial \rho_{ab}}{\partial t} = i\omega_{ab} - (1-\delta_{ab}) R_{ab,ab} \rho_{ab} - \delta_{ab} \sum_c R_{aa,cc} \rho_{cc}. \tag{3.20}$$

The elements of the Redfield matrix, Eq. 2.119, are calculated by inserting the expression for $\hat{H}_{SR}$, Eq. 3.15, into Eq. 2.118 for the damping matrix.

According to the established relation between the two representations (cf. Eq. 3.18), we are able to calculate the populations of the diabatic states

$$P_\alpha = \sum_{M_\alpha} \rho_{\alpha M_\alpha,\alpha M_\alpha} \tag{3.21}$$

As already mentioned, we aim at modelling the relaxation of the ν_s mode. Since the experiments showed that this process involves the ν_b mode, we will study its relaxation as well. To start with, we populated the states that have dominantly OH bending and stretching character (states $|\alpha = 5\rangle$ and $|\alpha = 20\rangle$, cf. Table 3.4) by means of a Frank-Condon like transition. The relaxation takes place via:

(i) Internal vibrational redistribution, which is due to the coupling terms $V_{\alpha\beta}$ that allow population transfer from $|\alpha\rangle$ to $|\beta\rangle$. According to the spectral density shown in Fig. 3.14, the energy cannot directly be transferred from ν_b and ν_s modes to the bath and therefore in the first step it is transfered to states that form the first tier. Fig. 3.11 suggests the the first tier for the ν_b/ν_s modes is formed by states ($|\alpha = 4\rangle$, $|\alpha = 6\rangle$ and $|\alpha = 7\rangle$)/($|\alpha = 15\rangle$, $|\alpha = 16\rangle$, $|\alpha = 17\rangle$, $|\alpha = 18\rangle$, $|\alpha = 19\rangle$ and $|\alpha = 21\rangle$).

(ii) Dissipation, which is accounted for through Eq. 3.15, i.e., via interactions with the internal and the external bath. The coupling strength for the linear interaction has previously been determined by classical MD simulations ($g^{(I)} = 0.057$), and the only parameter left to be determined in order to reproduce the experimentally observed relaxation time is the coupling strength for the third order interaction, $g^{(II)}$. For our calculations we used $g^{(II)} = 0.065$.

3.2.1 Relaxation Mechanism of ν_b

In order to study the relaxation mechanism of the ν_b mode, we populated the state $|\alpha = 5\rangle$ (cf. Table 3.4) which has dominantly OH bending character by means of a Frank-Condon like transition.

The diabatic state population dynamics is shown in Fig. 3.17. The blue line corresponds to the OH bending vibration. It decays monotonically, so that after 2 ps the population of state $|\alpha = 5\rangle$ was about 10%. The estimated IVR time τ_{IVR} = 850 fs is in a good agreement with the experimental results [91]. The green line represents sum of populations of the close lying states, which are essentially the overtones of ν_{γ_1} and ν_{γ_2} and their combination transition. The population is initially transferred to this manifold of states and it reaches the maximum after 400 fs. This population transfer is due to IVR, i.e., the energy stays within the system but is redistributed among different modes. The decay of the green line is accompanied with the rise of the red line that stands for the fundamental transitions of the

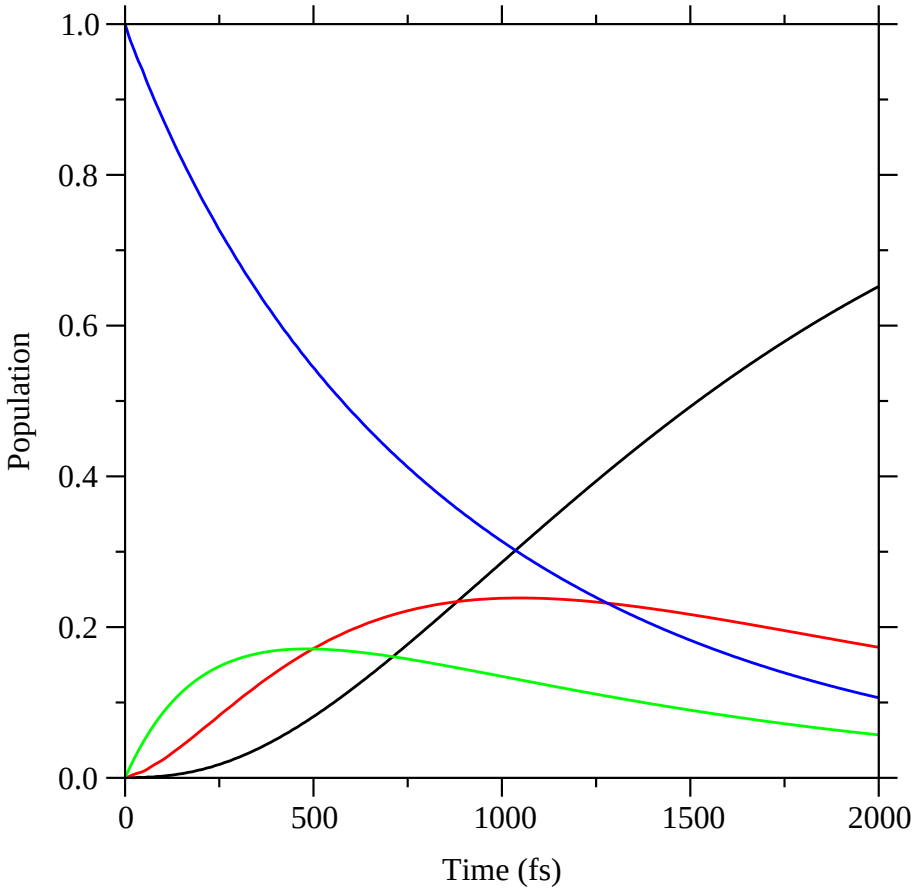

Figure 3.17: Population dynamics after a Frank-Condon like transition to the state $|\alpha = 5\rangle$ (blue line) which has essentially OH bending character. The green and the red line represent sums of $(P_4 + P_6 + P_7)$ and $(P_2 + P_3)$, respectively. The black line stands for the ground state.

two OH out-of-plane bending modes. This behavior is a consequence of the system - bath coupling. After 1 ps, those states get depopulated owing to the dissipation, Eq. 3.13. The ground state (black line) shows a uniform increase of population throughout the propagation.

This population/energy transfer is schematically shown in Fig. 3.18. The colors correspond to those of Fig. 3.17. It can clearly be seen that the system relaxes to the ground state by loosing one quantum of ν_{γ_1} and ν_{γ_2}, that further transfer the energy to the bath.

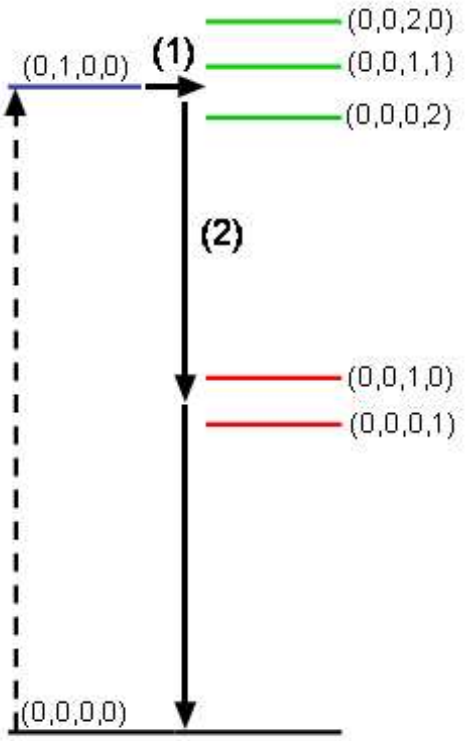

Figure 3.18: Stepwise energy transfer during the relaxation of the ν_b mode. The first step (1) is strongly influenced by the relaxation of the low frequency mode, while the second step (2) requires the third order relaxation mechanism.

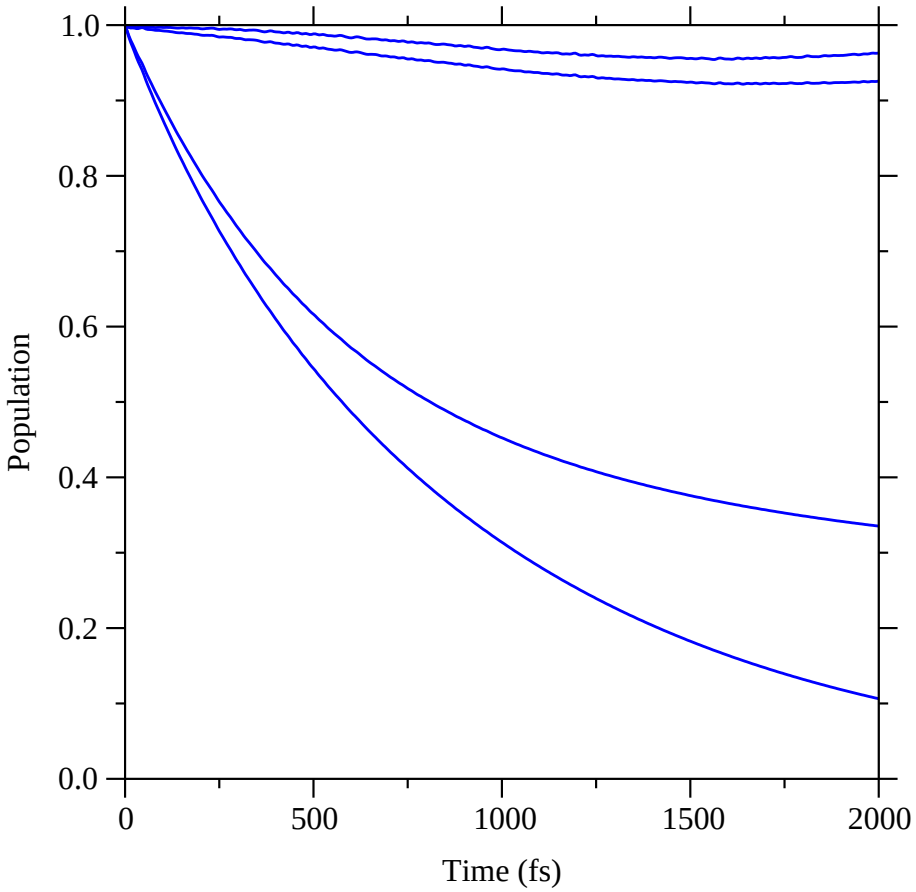

Figure 3.19: Populations of the state $|\alpha = 5\rangle$ after a Frank-Condon like transition under the following conditions (from bottom to top): by using the total Hamiltonian; without the 3rd order coupling; without the bilinear coupling; by neglecting both the internal and the external bath.

In order to understand the role of the bath, we performed a series of calculations under different conditions, Fig. 3.19. The Figure contains population changes of state $|\alpha = 5\rangle$. The lowest curve is obtained by using the total Hamiltonian, whereas for the next curve the 3rd order coupling is neglected. The importance of the intramolecular bath is apparent from Fig. 3.20 which contains changes of P_5 (blue), $(P_4 + P_6 + P_7)$ (green) and $(P_2 + P_3)$ (red): The population is transferred to the 1st tier (states marked with the green line in Fig. 3.18), but the system cannot relax to the ground state, since further energy release which can proceed only via the low frequency mode is too inefficient. Essentially, lower lying states do not have any influence on the dynamics, due to the fact that the last step from Fig. 3.18 is missing. This results in a much longer IVR time, τ_{IVR} = 1.5 ps.

The 3rd curve from bottom, Fig. 3.19, corresponds to the case when the bilinear coupling is neglected, i.e., the energy transfer from ν_{low} to the external bath is not applied. The population basically remains within the ν_b mode. This confirms the importance of the low frequency mode which facilitates an equilibration

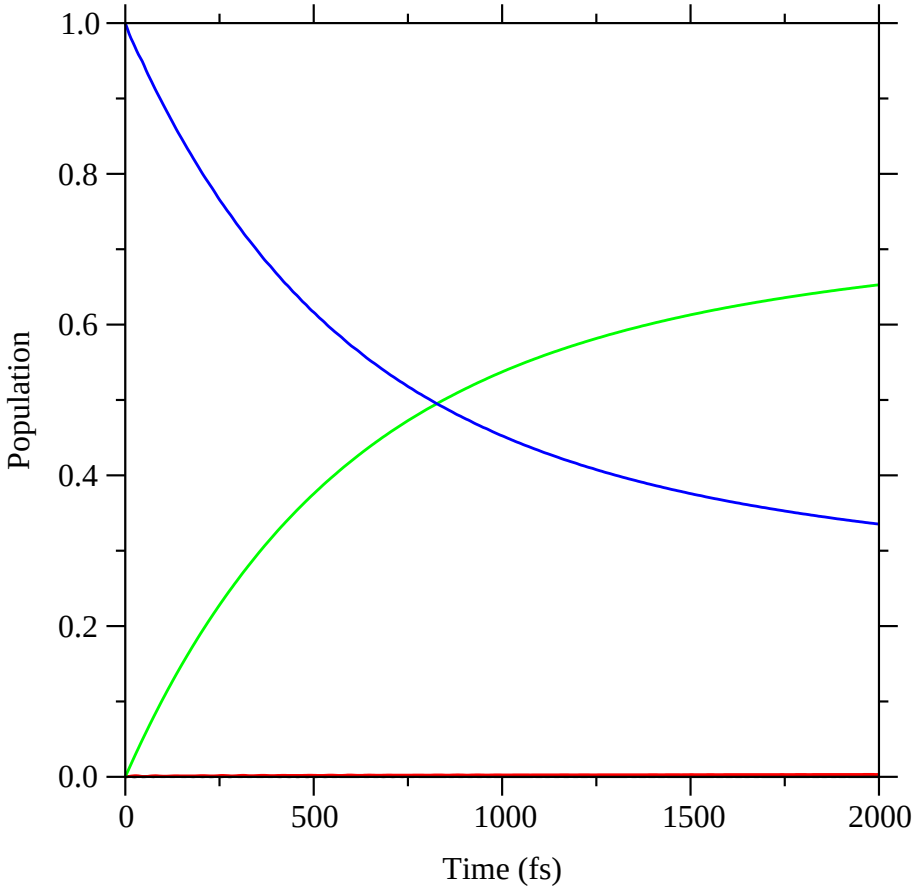

Figure 3.20: Populations changes of P_5, $(P_4 + P_6 + P_7)$ and $(P_2 + P_3)$ are represented with the blue, green and red line, respectively. For this calculation, the internal bath is neglected.

between those diabatic potential energy curves which are close in energy. Finally, the last curve in Fig. 3.19 describes the dynamics with no dissipation at all. Our results show that in order to reproduce the experimentally observed IVR time, it was necessary to introduce both the internal and the external bath.

3.2.2 Relaxation Mechanism of ν_s

We turn now to the investigation of relaxation of the OH stretching vibration. The question arises whether we can use the same parameters as for the bending excitation. Like in the previous case, the state that has dominantly OH stretching character, $|\alpha = 20\rangle$ is initially populated by a Frank-Condon transition, and the population changes of the relevant states are depicted in Fig. 3.21. The nature of states being (de)populated can best be viewed by comparing with the energy levels sketched in Fig. 3.22. The population is directly transferred to the 1^{st} tier, which consists of states (0,1,2,0), (0.1,1,1), (0,2,0,0) and (0,1,0,2) (marked with a yellow color). The second step includes population transfer to (0,1,1,0) and (0,1,0,1),

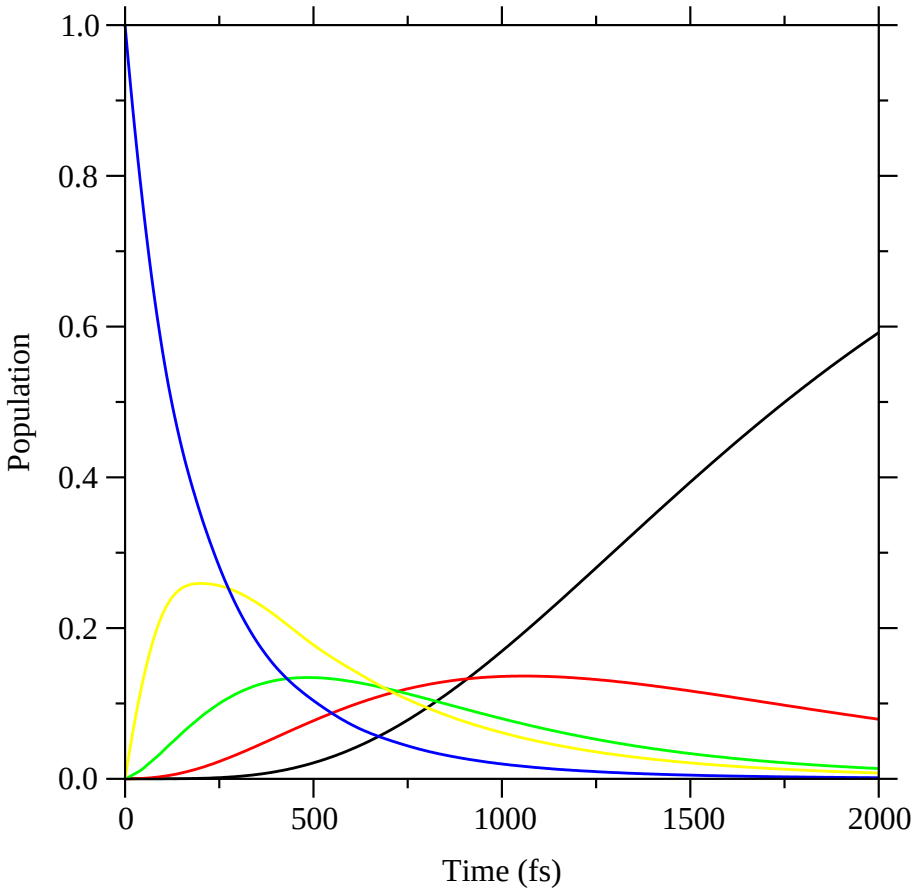

Figure 3.21: Population dynamics after a Frank-Condon like transition to the state $|\alpha = 20\rangle$ (blue line) which has essentially OH stretching character. The yellow and the green line represent sums of $(P_{15} + P_{16} + P_{18} + P_{21})$ and $(P_9 + P_{11})$, respectively, whereas the red line corresponds to P_5. The black line stands for the ground state.

whereas in the next step the fundamental OH bending mode is excited, as well as the close lying states. Further relaxation proceeds via the mechanism explained in the previous section. In other words, the relaxation of the OH stretching mode is a cascading process, which takes place via release of one quantum of energy of ν_{γ_1} and ν_{γ_2}, in each step, Fig. 3.22. The estimated IVR time is τ_{IVR} = 190 fs which is in good accord with the experimental value [91].

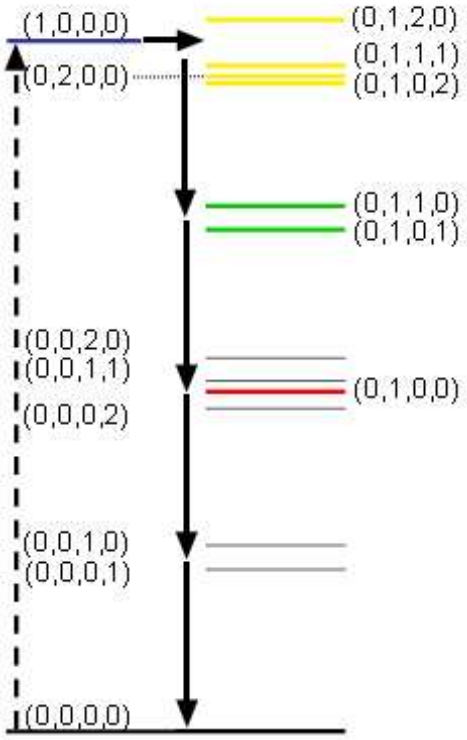

Figure 3.22: Cascaded energy transfer during the relaxation of the ν_s mode. The population is initially transfered from the state $|\alpha = 20\rangle$ to the closest states displayed with the yellow color. This manifold of states is composed from the bending overtone, as well as the combinations of ν_b with the overtones of ν_{γ_1} and ν_{γ_2}. As in the previous case (relaxation of the ν_b mode) this first step takes place due to the presence of ν_{low}. Further energy release proceeds via the internal bath.

Let us consider the effect of the bath in more detail, Fig. 3.23. If the internal bath is not accounted for, 2$^{\text{nd}}$ curve from the bottom, the relaxation time for the ν_s mode is 200 fs, which still reproduces the experimental value well. That means that 3$^{\text{rd}}$ order coupling does not strongly affect population decrease from $|\alpha = 20\rangle$ state, since the energy is in the first step dominantly transferred to four neighboring states, Fig. 3.24. Due to the low ν_{low}, the population is transferred to the first tier (yellow line) formed by the closest states. According to Table 3.4, they involve the overtone of ν_b, as well as the combination of ν_b and the overtones of ν_{γ_1} and ν_{γ_2}. However, further energy release would include loss of energy that corresponds to the OH out of plane modes, and for this purpose the internal bath is required. Since this channel for relaxation is not accounted for, those states do not take place in the dynamics. In other words, fast relaxation of the $|\alpha = 20\rangle$ state is due to IVR, i.e., strong coupling to the close diabatic levels that results in popu-

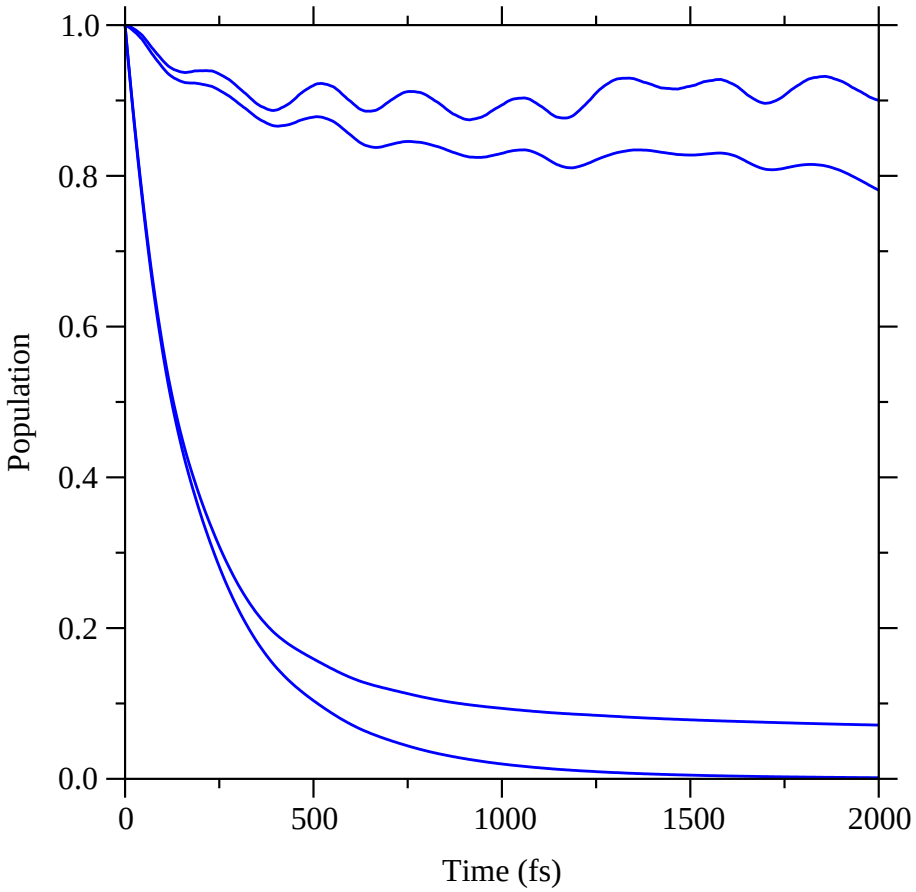

Figure 3.23: Populations of the state $|\alpha = 20\rangle$ after a Frank-Condon like transition under the following conditions (from bottom to top): by using the total Hamiltonian; without the 3$^{\text{rd}}$ order coupling; without the bilinear coupling; by neglecting both the internal and the external bath.

lation transfer. Those *intramolecular* couplings are stronger than the *intermolecular* with the internal bath, so the presence of the later is not necessary for getting a crude explanation of this process. Nevertheless, the external bath plays again a crucial role: The neglection of the bilinear coupling, 3$^{\text{rd}}$ curve from the bottom, leads to an extremely slow population decay.

Analysis of the OH stretching vibration of HOD in liquid D_2O [89], [90] showed that it takes place via the overtone of the OH bending vibration. Since the PMME molecule is larger, more degrees of freedom take part in the dynamics, and the mechanism includes in addition to the in plane bending overtone states formed by combinations with the two OH out of plane bending modes. That is, due to the greater complexity of the system, more resonance transitions appear, which results in a different relaxation pathway.

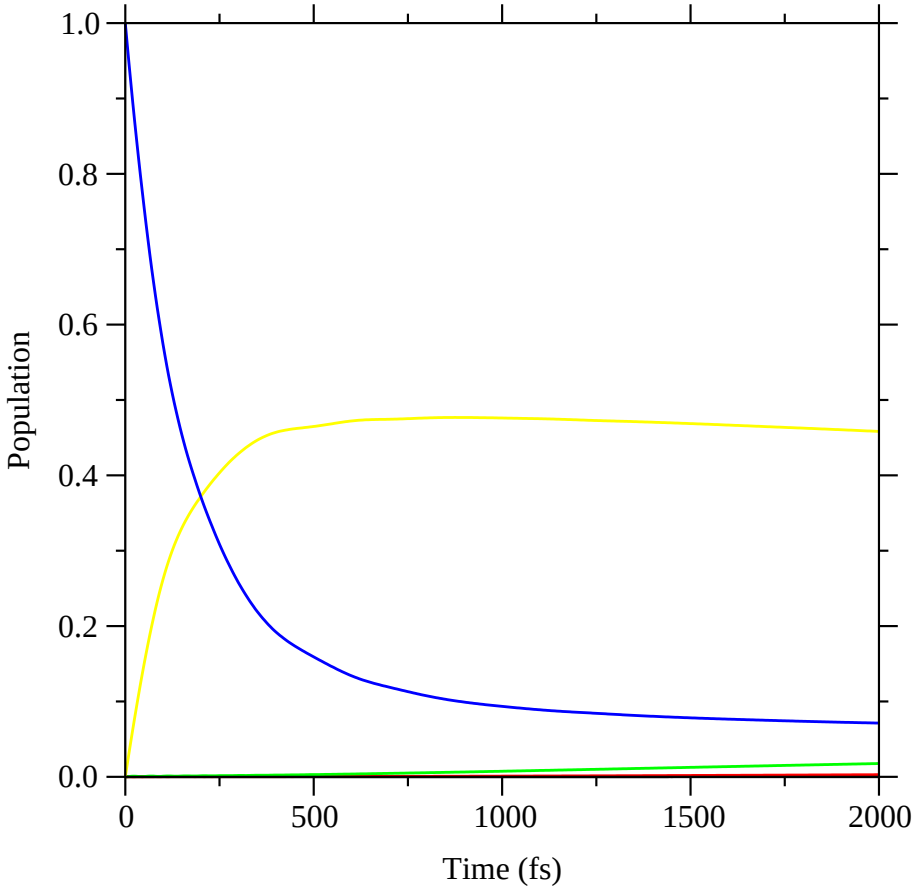

Figure 3.24: Populations changes of P_{20}, $(P_{15}+P_{16}+P_{18}+P_{21})$, (P_9+P_{11}) and P_5 are represented with the blue, yellow, green and red line, respectively. For this calculation, the internal bath is neglected.

3.2.3 Concluding Remarks

We studied the relaxation mechanisms of the OH bending and stretching vibrations in PMME. Both modes cannot release the energy directly to the bath, due to the absence of resonant transitions of the bath modes. Therefore, they transfer the energy to the neighboring states. This step is supported by the low frequency mode, which directly interacts with the external bath. The relaxation of the OH out of plane modes takes place via a 3$^{\text{rd}}$ order process, which includes both the internal bath (which consists of two molecular modes) and the external bath. The coupling strength for the relaxation of ν_{low} was previously determined, and the only parameter we introduced was the coupling strength for the 3$^{\text{rd}}$ order process. We used the same value for $g^{(II)}$ for modelling the relaxation of ν_b and ν_s. The present model could be extended by using, for instance, full Redfield equations. Further, the Frank-Condon like transition could be replaced by an excitation with an IR laser pulse. Due to its finite width, the pulse would excite not just state $|\alpha = 20\rangle$, but the whole manifold.

The proposed mechanism represents only one channel for relaxation. It was experimentally observed that 30% of population of ν_s relaxes via ν_b. Therefore, we focused our attention on the most important pathway, although a molecule that contains as many degrees of freedom as PMME, can probably relax through different mechanisms. We believe that such cascading relaxation is not a property of this specific molecule, but rather represents a generic behavior of intramolecular hydrogen bonded systems. For example, τ_{IVR} of the deuterated 2-(2'-hydroxophenyl)benzothiazole is also estimated to be about 200 fs [97].